ORIGINAL RESEARCH ARTICLE

Fracture Resistance of Advanced High-Strength Steel Sheets for Automotive Applications

D. FRÓMETA, A. LARA, L. GRIFÉ, T. DIEUDONNÉ, P. DIETSCH, J. REHRL, C. SUPPAN, D. CASELLAS, and J. CALVO

The fracture resistance of different advanced high-strength steel (AHSS) sheets for automotive applications is investigated through conventional tensile tests, fracture toughness measurements, and hole expansion tests. Different fracture-related parameters, such as the true fracture strain (TFS), the true thickness strain (TTS), the fracture toughness at crack initiation (w_e^i), the specific essential work of fracture (w_e), and the hole expansion ratio (HER), are assessed. The specific essential work of fracture (w_e) is shown to be a suitable parameter to evaluate the local formability and fracture resistance of AHSS. The results reveal that fracture toughness cannot be estimated from any of the parameters derived from tensile tests and show the importance of microstructural features on crack propagation resistance. Based on the relation fracture toughness-local formability, a new AHSS classification mapping accounting for global formability and cracking resistance is proposed. Furthermore, a physically motivated fracture criterion for edge-cracking prediction, based on thickness strain measurements in fatigue pre-cracked DENT specimens, is proposed.

https://doi.org/10.1007/s11661-020-06119-y

I. INTRODUCTION

ADVANCED high-strength steels (AHSS) play a fundamental role in the development of modern lightweight automobiles. The use of these steels for structural and safety related automotive components is undergoing a continuous increase in the last years. The body structure of current passenger cars can have up to 51 pct of AHSS[1] and this percentage might grow up to 65 pct in upcoming vehicles.[1,2] The main advantage of AHSS is their excellent combination of high strength and good ductility, which has significantly contributed to reduce the total vehicle mass, while improving crash performance.

The AHSS family comprises a wide variety of complex multiphase microstructures that provide unique combinations of mechanical properties by adjusting their chemical composition and thermomechanical processing routes. AHSS are categorized into three main groups or families: 1st-, 2nd-, and 3rd-generation AHSS.[1] Dual phase (DP), complex phase (CP), martensitic (MS), press-hardened (PHS), and transformation-induced plasticity (TRIP) steels are part of the 1st generation of AHSS. This generation is characterized by showing higher strength and formability than single-phase high-strength low-alloyed (HSLA) steels.[3] The 2nd generation includes twinning-induced plasticity (TWIP) and austenitic steels. These steels present excellent ductility compared to the 1st-generation AHSS at similar strength levels. However, their high alloy content, which significantly increases production costs, and other problems related to delayed fractures and poor weldability have limited their application.[4] The 3rd generation arose to cover the gap between the 1st and the 2nd generation of AHSS. These steels exhibit higher strength and formability than the 1st generation of steels at significantly lower costs than the 2nd generation of steels.[1] Some of the steels developed under this classification are TBF (TRIP-aided bainitic ferritic) and Q&P (quenching and partitioning) steels. Other TRIP-assisted steels, such as medium-Mn[5] or δ-TRIP steels,[6] and nanoprecipitation steels[7] are under development.

D. FRÓMETA, A. LARA and L. GRIFÉ are with the Unit of Metallic and Ceramic Materials, Eurecat, Centre Tecnològic de Catalunya, Plaça de la Ciència, 2, 08243 Manresa, Spain. T. DIEUDONNÉ and P. DIETSCH are with the ArcelorMittal Maizières Research SA, Voie Romaine, BP30320, 57283 Maizières-les-Metz, France. J. REHRL and C. SUPPAN are with the Voestalpine Stahl GmbH, Voestalpine-Straße 3, 4020 Linz, Austria. D. CASELLAS is with the Unit of Metallic and Ceramic Materials, Eurecat, Centre Tecnològic de Catalunya and also with the Division of Mechanics of Solid Materials, Luleå University of Technology, 971 87 Luleå, Sweden. Contact e-mail: daniel.casellas@ltu.se J. CALVO is with the Universitat Politècnica de Catalunya, Materials Science and Engineering department, Eduard Maristany 16, 08019 Barcelona, Spain.

Manuscript submitted August 4, 2020; accepted November 12, 2020.

Article published online January 3, 2021

The development of new AHSS with higher strength has introduced new forming challenges and fracture problems related to their limited cracking resistance, as, for example, edge fractures, limited hole expandability, *and so on*.[8–10] Often, these fractures are not coherent with conventional formability criteria based on elongation values from tensile tests or forming limit curves (FLC).[8] A clear example is the edge formability of DP and CP steels. DP steels usually show lower edge formability and hole expansion ability than CP steels, even though the former have greater uniform and total elongation and higher limit strains in the FLC.[9,11–15] This inconsistency between fracture resistance and traditional ductility definitions motivated the development of new formability criteria for AHSS, differentiating between global and local formability.[16,17] The term global formability refers to the most traditional interpretation of formability, *i.e.*, the resistance against the onset of necking instability, and it is well described by tensile properties (strain hardening exponent, true uniform strain) and FLC. On the other hand, local formability is linked to the material's damage tolerance and cracking resistance (bendability, edge cracking, hole expansion, *etc.*) and, as mentioned before, has no apparent relation with tensile strength/ductility properties. Consequently, alternative approaches have been developed to experimentally assess the local formability of AHSS. The hole expansion test (HET) according to ISO 16630[18] is well established as a standard procedure for stretch flangeability evaluation of AHSS sheets and the hole expansion ratio (HER) has become an almost mandatory parameter for AHSS products manufacturers. Nevertheless, the HER is not a material property and depends on many external factors that can cause large data scattering and compromise its reliability: hole preparation method, edge quality, tool stiffness, test operator, crack detection method, *etc.*[11,15,19–24] In order to overcome such uncertainties and improve the accuracy of edge formability prediction, a series of alternative tests based on optical strain measurements and digital image correlation (DIC) techniques have been proposed.[15,24–29]

More recently, other authors have suggested the use of local fracture strain measurements from uniaxial tensile specimens, such as the true fracture strain (TFS or ε_f),[16] the reduction of area (Z-value),[30] or the true thickness strain (TTS),[17,30] as an indicator of local formability of AHSS. Hance[16] proposed the TFS derived from the reduction of area fracture surface to assess the fracture resistance of AHSS sheets and, on the basis of this parameter, developed enhanced formability mappings and defined different performance levels for AHSS.[16,31] Larour *et al.*[30] and Heibel *et al.*[17] observed a very good correlation between the TTS and the HER of several AHSS grades. Following the idea of Hance, Heibel *et al.* proposed a new classification of AHSS according to their global and local ductility, using the true uniform strain and the TTS, respectively.[17]

By definition, local formability is related to the material's crack nucleation and propagation resistance, *i.e.,* its fracture toughness. Accordingly, other researchers have used different approaches based on fracture mechanics testing for fracture resistance and local ductility assessment of AHSS.[9,14,15,32–35] For instance, Takahashi *et al.*[32] investigated stretch flangeability of different hot-rolled high-strength steels and found a linear correlation between J_c and HER. Similar correlation between fracture toughness values and HER was observed by Casellas *et al.*,[14] Yoon *et al.*,[33] and Frómeta *et al.*[9,15]. In References 34 and 35, a link was established between crack propagation resistance and crash folding behavior and other local ductility parameters for several AHSS grades (V-bending, local fracture strain from DIC, *etc.*).

Following such research, the present work aims at providing further evidence on the relationship between fracture toughness and cracking resistance of AHSS and proposes a new fracture performance classification for AHSS according to their crack propagation resistance. The fracture resistance of different 1st- and 3rd-generation AHSS steel grades with ultimate tensile strengths (UTS) from 780 to 1180 MPa is investigated by means of uniaxial tensile tests, essential work of fracture tests, and hole expansion tests. The correlation between the different parameters is investigated and the role of the main microstructural characteristics on fracture performance is discussed. The microstructure–material performance relationship is addressed by using the fracture toughness and fracture strain values derived from these tests, because such properties are well correlated to edge cracking and impact crack propagation behavior.[9,14,15,34,35] Based on such analysis, a global ductility vs. fracture toughness diagram is presented to describe the overall formability and fracture resistance of AHSS.

II. MATERIALS AND METHODS

A. *Materials*

Six cold-rolled AHSS grades in the range of 780 to 1180 MPa UTS are investigated. The steels were manufactured and supplied by voestalpine Stahl and ArcelorMittal. Table I classifies the 6 AHSS grades according to their strength level and AHSS generation. The steel supplier is also indicated. All the steels were provided in the form of 1.4 to 1.6 mm thick sheets, except for the 3rd Gen DP1180 (t = 1.2 mm). Microstructures are shown in Figures 1, 2, and 3. The figures show optical micrographs after LePera etching and scanning electron microscope (SEM) images. The chemical compositions and the microstructural constituents are given in Tables II and III, respectively. The retained austenite (RA) volume fraction was measured *via* the saturation magnetization method, as explained in Reference 36.

780 MPa grades show a matrix mainly consisting of ferrite (F) and bainite (B) with different amounts of martensite (M) and martensite/retained austenite (M/RA) islands. DP780 has a lower amount of RA when compared to the TRIP780 grade. On the other hand, DP980 has a ferritic–bainitic matrix with some amount of tempered martensite and a lower amount of hard martensite islands, which are finely distributed.

Table I. Description of the Investigated AHSS Grades

AHSS Generation	Strength Level (MPa)	Steel Denomination	Thickness (mm)	Supplier
1st GEN	780	DP780	1.5	Voestalpine
		TRIP780	1.6	ArcelorMittal
	980	DP980	1.35	Voestalpine
3rd GEN	1180	3rd Gen DP1180	1.2	Voestalpine
		3rd Gen TBF1180	1.4	ArcelorMittal
		3rd Gen Q&P1180	1.5	ArcelorMittal

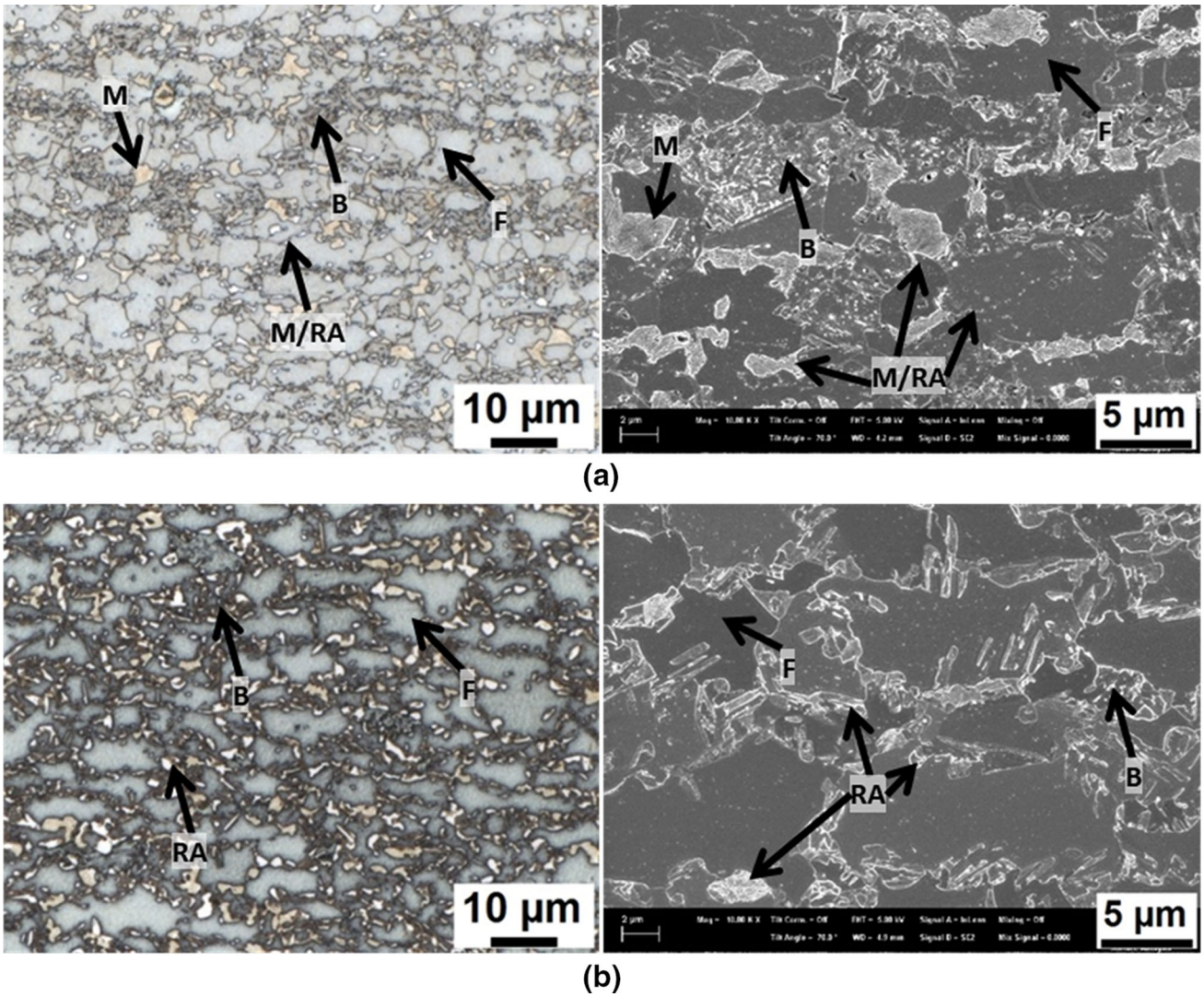

Fig. 1—Micrographs of 780 MPa steel grades. Left: Optical microscopy with LePera etching. Right: SEM. (*a*) DP780. (*b*) TRIP780.

3rd Gen DP1180 both consists of a matrix of partly upper bainite (UB) with globular islands of M/RA, and partly of lower bainite/tempered martensite (LB/TM) with globular and lamellar formed islands of M/RA. The 3rd Gen TBF1180 is composed of a matrix of carbide-free bainite with globular islands of M/RA and laths of RA. However, the structure of the 3rd Gen TBF1180 is a bit coarser than the one of 3rd Gen DP1180, which might be attributed to a larger size in prior austenite grains. The microstructure of the grade 3rd Gen Q&P1180 is significantly different when compared to the 3rd Gen DP1180 and TBF1180 steels. It has a matrix consisting of tempered or carbon-depleted martensite, including lath-like retained austenite, globular islands of M/RA and bainite. All three 1180MPa grades show quite high contents of retained austenite (12 to 16 pct).

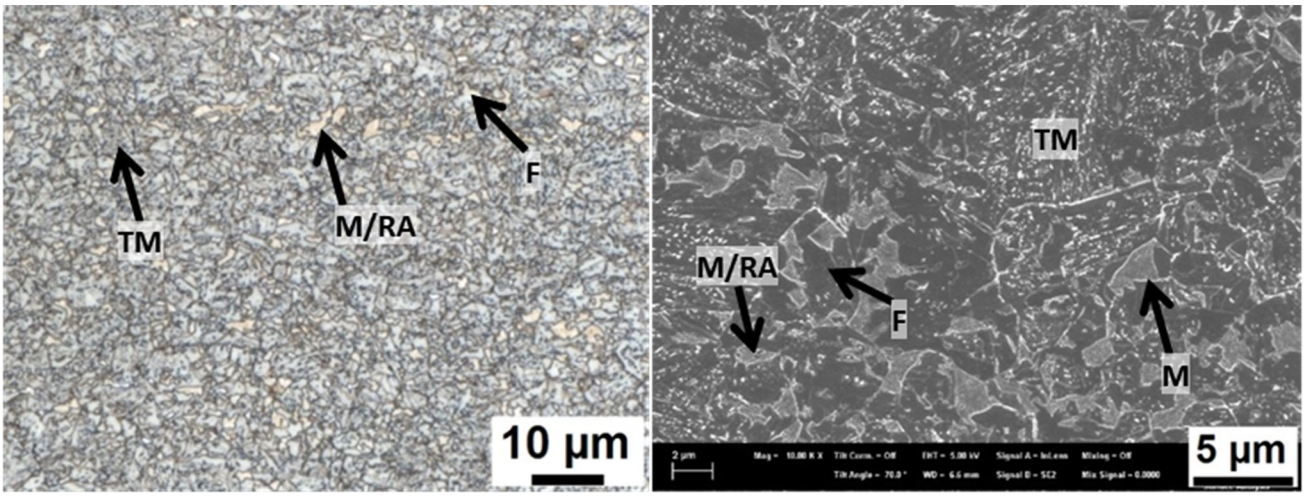

Fig. 2—Micrographs of DP980. Left: Optical microscopy with LePera etching. Right: SEM.

B. *Experimental Procedure*

1. *Uniaxial tensile tests*

Conventional uniaxial tensile tests were performed according to ISO 6892-1.[37] Standard tensile specimens with a parallel length of 120 mm and a width of 20 mm were machined at transverse orientation with respect to the rolling direction. An initial gauge length of 80 mm was used for elongation measurements and 3 specimens per material were tested.

The true fracture strain (TFS), derived from the reduction of area at the fracture location, was evaluated according to Eq. [1]:

$$\mathrm{TFS} = \ln\left(\frac{A_0}{A_f}\right) \quad [1]$$

where A_0 is the initial cross-section area and A_f is the area at fracture. The area at fracture was measured from the fracture surface of the tensile specimens according to ASTM E8[38] with an optical microscope. Thickness measurements were performed on the left (t_{left}) and right (t_{right}) edges and in the middle of the fracture surface (t_{mid}) (Figure 4). From this, the thickness at fracture (t_f) was obtained as follows:

$$t_f = \frac{1}{6}\left(t_{left} + 4t_{mid} + t_{right}\right) \quad [2]$$

A_f is calculated according to Eq. [3]:

$$A_f = \mathrm{width}_f * t_f \quad [3]$$

where width_f is the width of the fractured area (Figure 4).

The true thickness strain (TTS) was calculated using Eq. [4]:

$$\mathrm{TTS} = \ln\left(\frac{t_0}{t_f}\right) \quad [4]$$

where t_o is the initial sheet thickness.

2. *Fracture toughness*

The fracture toughness of the studied AHSS grades was evaluated by means of the essential work of fracture (EWF) methodology.[39] The method allows to experimentally separate the ductile fracture energy (W_f) into two energetic contributions, as shown in Eq. [5].

$$W_f = W_e + W_p = w_e l_0 t_0 + w_p \beta l_0^2 t_0 \quad [5]$$

where W_e is the essential work of fracture developed in the fracture process zone and W_p is the non-essential plastic work dissipated in an outer region surrounding the crack plane. w_e is the specific work of fracture per unit area, l_0 is the ligament length, t_0 is the specimen thickness, w_p is the specific non-essential plastic work per unit volume, and β is a shape factor that depends on the shape of the plastic zone. Dividing Eq. [5] by the initial cross-section area ($l_0 t_0$) gives:

$$\frac{W_f}{l_0 t_0} = w_f = w_e + w_p \beta l_0 \quad [6]$$

According to Eq. [6], if a series of specimens with different ligament lengths is tested up to fracture and w_f is plotted against the ligament length (l_0), a straight line is obtained. Then, w_e can be determined by linear extrapolation to zero ligament length. w_e has shown to be a suitable parameter to describe the crack propagation resistance of thin ductile sheets, including polymers,[40–42] metals,[43–47] and AHSS.[9,14,15,34,35,48–52] It is important to point out that the plane stress fracture toughness of thin ductile sheets has an important contribution from necking and, therefore, the measured w_e cannot be considered an intrinsic material property but a material constant for the given sheet thickness.

Even though w_e has shown to be independent of the specimen geometry and can be obtained from different geometries,[40,42] for thin sheets, the EWF testing protocol[53] developed by the European Structural Integrity Society (ESIS) recommends the use of double edge notched tension (DENT) specimens because of its

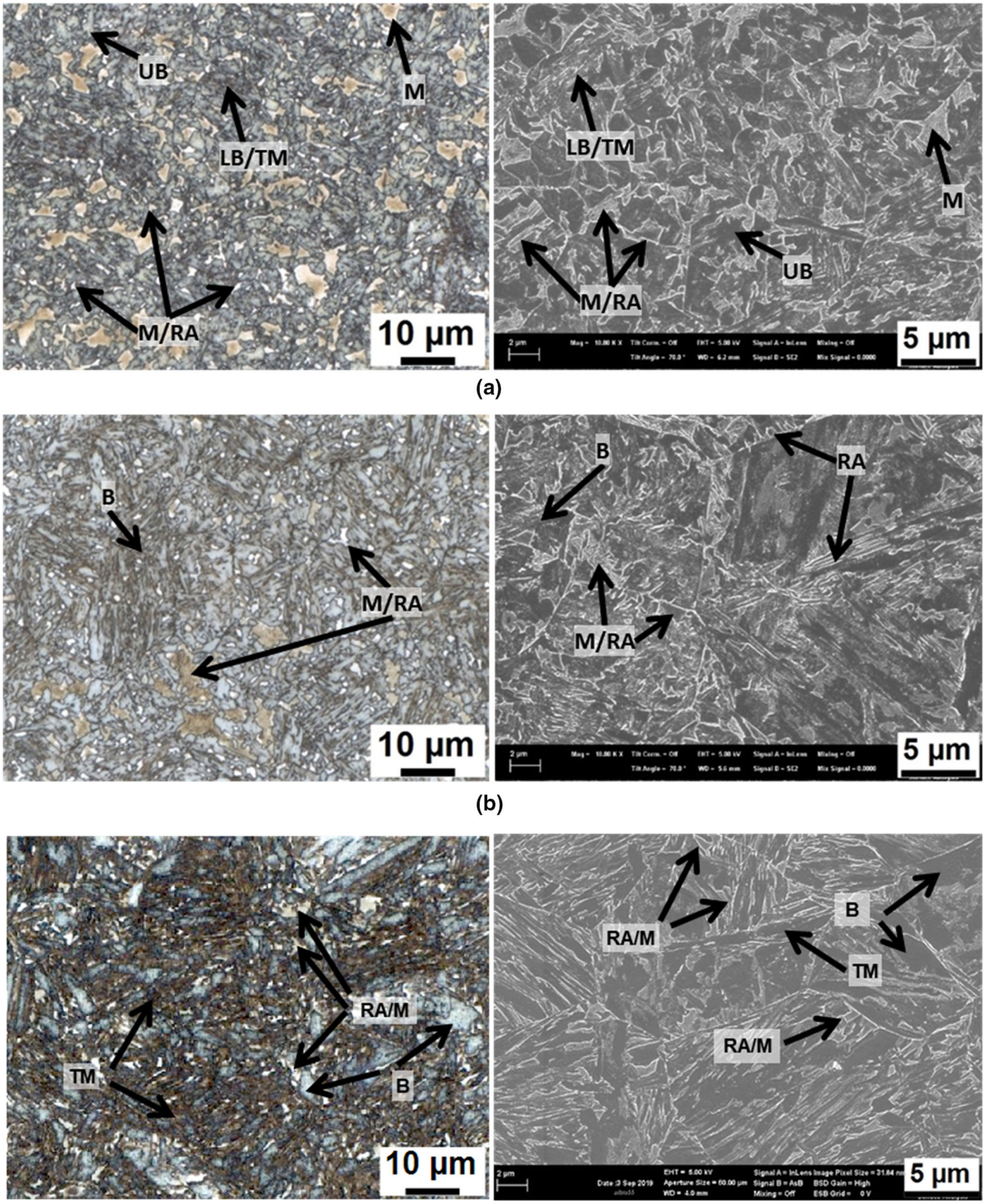

Fig. 3—Micrographs of 1180 MPa steel grades. Left: Optical microscopy with LePera etching. Right: SEM. (*a*) 3rd Gen DP1180, (*b*) 3rd Gen TBF1180, and (*c*) 3rd Gen Q&P1180.

Table II. Chemical Composition (in Weight Pct, the Balance Is Fe)

Steel Grade	C	Si	Mn	Cr	B	Al	Ti
DP780	~ 0.15	< 0.9	< 2.0	< 0.7	< 0.003	~ 0.05	< 0.0060
TRIP780	~ 0.20	~ 1.60	~ 1.70	~ 0.02	< 0.001	~ 0.05	~ 0.0070
DP980	~ 0.15	< 0.5	~ 2.3	< 0.7	< 0.003	~ 0.05	< 0.0060
3rd Gen DP1180	~ 0.20	< 2.0	~ 2.5	< 0.7	< 0.003	~ 0.05	< 0.0060
3rd Gen TBF1180	~ 0.23	< 2.0	< 2.9	< 0.7	< 0.005	~ 0.04	~ 0.0070
3rd Gen Q&P1180	~ 0.18	< 2.0	< 2.9	< 0.7	< 0.005	~ 0.03	~ 0.0060

Table III. Microstructural Constituents

Steel	Microstructure	RA Volume Fraction, $V\gamma$ (Pct)
DP780	F/B matrix, M/RA islands	9.8
TRIP780	F/B matrix, M/RA islands	15.6
DP980	F/B matrix, TM, M islands, RA	5.5
3rd Gen DP1180	UB/LB matrix, M/RA islands and laths	14.8
3rd Gen TBF1180	carbide-free B matrix, M/RA islands and laths of RA	15.5
3rd Gen Q&P1180	TM matrix, B, M/RA islands and laths of RA	12.6

F ferrite, *B* bainite, *M* martensite, *TM* tempered martensite, *RA* retained austenite, *UB* upper bainite, *LB* lower bainite.

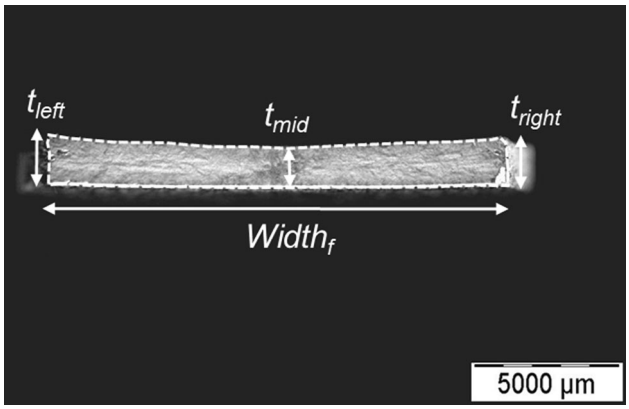

Fig. 4—Fracture surface of a uniaxial tensile specimen and location of the thickness and width measurements performed to evaluate the TFS and the TTS. The dashed line represents the contour of the fractured area.

symmetry and minimal specimen rotation and buckling during testing.

In the present work, EWF tests were performed by testing rectangular DENT specimens with dimensions of 240 × 55 mm machined in the transverse orientation with respect to the rolling direction (notches aligned in the rolling direction). Five different initial ligament lengths (l_0) ranging from 6 to 14 mm were used and 3 specimens per ligament length were tested. The specimens were tested up to fracture at a constant cross-head speed of 1 mm/min. Initial notches were machined by electrical discharge machining (EDM) and fatigue pre-cracks were nucleated at the notch root to avoid the effect of the notch radius on fracture toughness results (Figure 5(a)).

The fracture toughness at crack initiation (w_e^i) was also assessed by calculating the energy up to the onset of crack propagation as described in References 34 and 51. Further details about the experimental procedure for the determination of the EWF in AHSS sheets are published in previous works.[14,34,35,49–51]

The thickness strain of the DENT specimens was evaluated according to Eq. [7]:

$$\varepsilon_{3fDENT} = \ln\left(\frac{t_0}{t_f}\right) \quad [7]$$

where t_o is the initial sheet thickness and t_f is the thickness at fracture measured from the fracture surface (Figure 5(b)). The thickness measurements were performed at different locations and the evolution of $\varepsilon_{3f\,DENT}$ as a function of the distance from the crack tip was evaluated.[51] Two different terms were identified: the thickness strain at crack initiation ($\varepsilon^i_{3f\,DENT}$) and the thickness strain for the stable crack propagation ($\varepsilon_{3f\,DENT}{}^p$).

3. *Hole expansion tests*

Hole expansion tests (HET) were performed according to ISO 16630.[18] Square samples 100 × 100 mm with an initial punched hole 10 mm in diameter in the center were used (Figure 6(a)). According to standard recommendations, the hole was punched using a punch-to-die clearance of 12 ± 2 pct. The hole expansion was performed using a conical expansion tool with a top angle of 60 deg. The tests were conducted in a universal testing machine at displacement rate of 1 mm/s and were stopped after the first through-thickness crack was observed. Crack formation was detected by using a high-resolution video camera (Figure 6). A minimum of 5 specimens per material were tested. The limiting hole expansion ratio (HER) was obtained as follows:

$$HER = \frac{D_h - D_0}{D_h} \times 100 \quad [8]$$

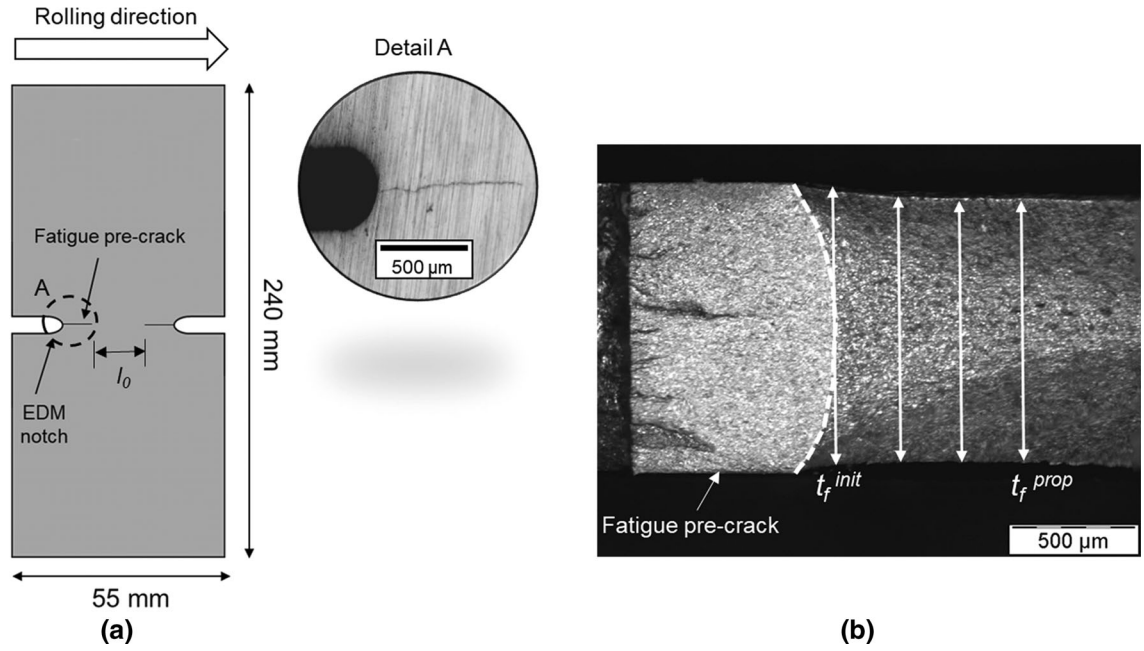

Fig. 5—(*a*) DENT specimen used for EWF tests and detail of the fatigue pre-crack at the notch root. (*b*) Fracture surface of a DENT specimen and location of the different thickness measurements. The dashed line indicates the crack tip.

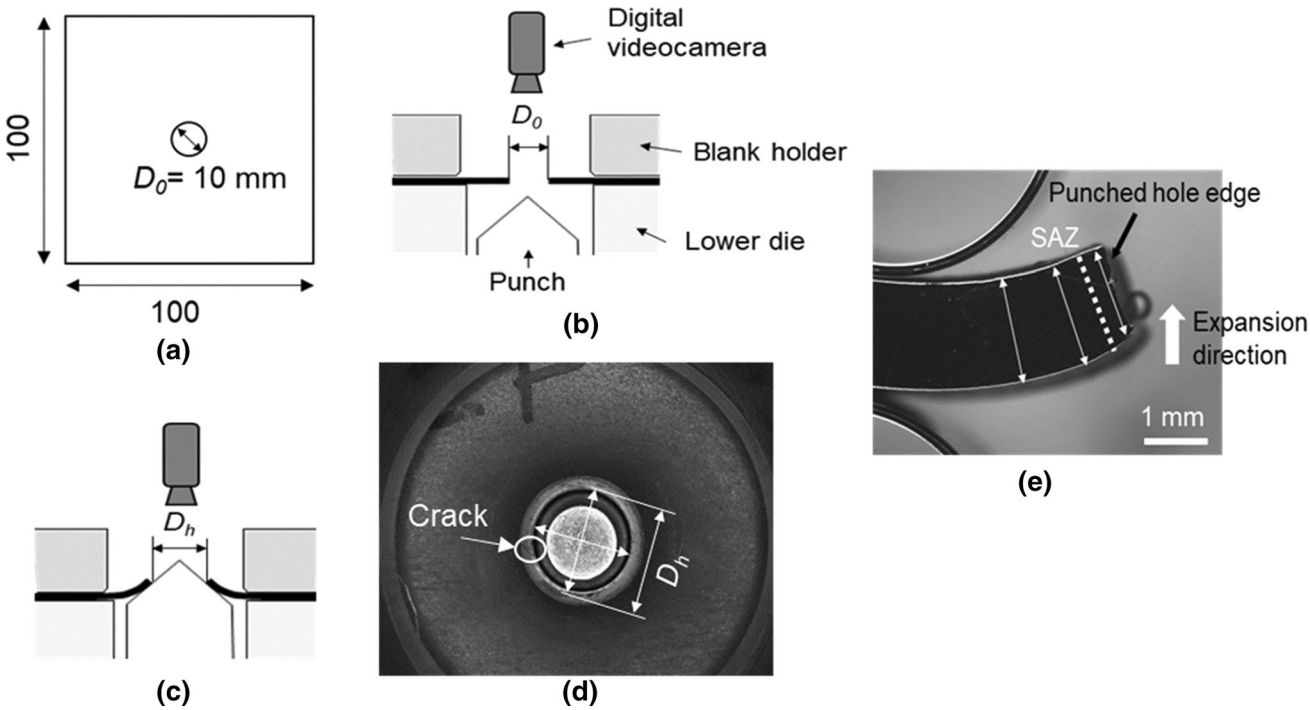

Fig. 6—(*a*) Specimen geometry for HET. (*b*, *c*) Schematic representation of the experimental procedure for the HET. Before (b) and after (c) the test. (*d*) Digital image used for the evaluation of the HER. (*e*) Longitudinal section of a crack in a HET specimen after the test and location of the thickness measurements performed. SAZ: shear-affected zone.

where D_h is the hole diameter after failure and D_0 is the initial hole diameter. D_h was measured from the images of the video camera by using a digital image analysis software (Figure 6(d)).

Furthermore, thickness measurements at the crack edge were performed by sectioning the cracks of HET specimens after the test, as suggested in Reference 54. Figure 6(e) shows a longitudinal section of a crack and the thickness measurements performed at different

distances from the punched hole edge. Thickness strains were calculated in the same manner as described above for DENT specimens (Eq. [7]).

III. RESULTS

A. *Uniaxial Tensile Properties*

Figure 7 shows the engineering and true stress–strain curves for the 6 AHSS grades investigated. True stress–strain curves are represented up to the uniform strain and linearly extrapolated to the true fracture strain. The fracture stress was calculated by dividing the load at fracture by the fracture area. The mechanical properties are summarized in Table IV.

DP780 shows comparable YS and UTS but lower elongation (both uniform and total) and UTSxTE than TRIP780. Both steels also show similar strain hardening exponent (calculated between 2 and 4 pct of deformation) and TFS. DP980 shows higher strength and lower elongation than 780 MPa steel grades. However, it exhibits higher TFS. Despite their higher strength, 3rd Gen 1180 MPa steel grades show greater uniform and total elongation values than DP980. The 3rd Gen DP1180 presents lower YS, slightly higher UE/TE, and the same UTS level than 3rd Gen TBF1180. 3rd Gen Q&P1180 has similar elongation to 3rd Gen TBF1180 but higher YS and slightly lower UTS. 3rd Gen DP1180 shows the greatest UTSxTE product of the three 1180 MPa grades. On the other hand, 3rd Gen Q&P1180 shows the greatest TFS of the investigated steel grades.

B. *Fracture Toughness*

1. *Essential work of fracture*

Figure 8 shows the results from EWF tests. w_e and w_e^i values are given in Table V. TRIP780 shows one of the lowest w_e of the investigated steels, comparable to that of 3rd Gen DP1180 and 3rd Gen TBF1180. DP780 has slightly greater w_e, similar to DP980 ($w_e \approx 150$ kJ/m^2). 3rd Gen Q&P1180 presents the greatest w_e. Concerning the fracture toughness at crack initiation, the trend is similar to the one observed for w_e. TRIP780, 3rd Gen

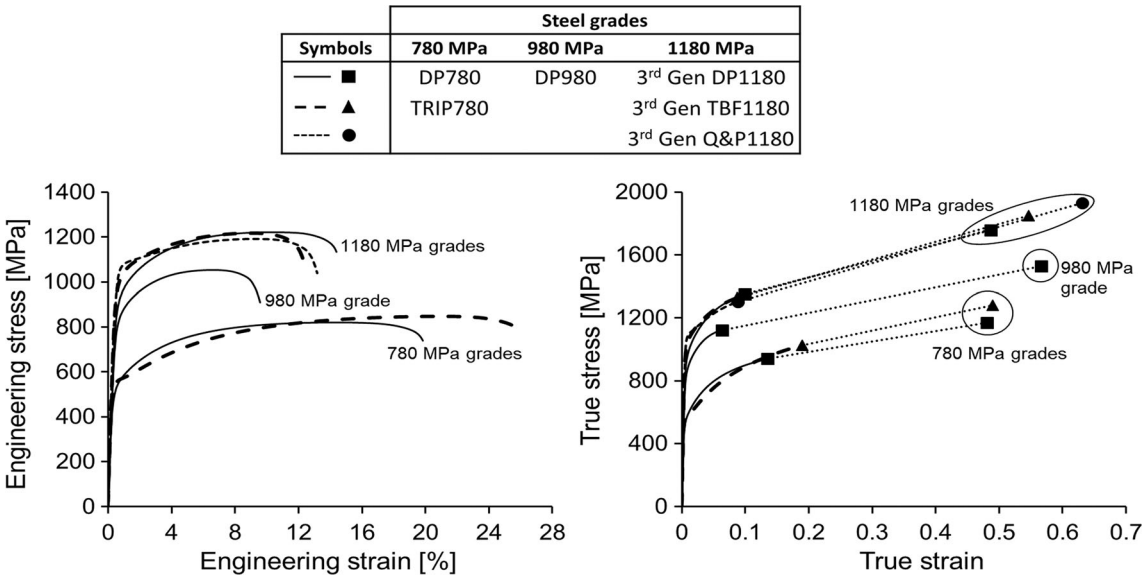

Fig. 7—Engineering (left) and true (right) stress–strain curves for the investigated AHSS grades.

Table IV. Mechanical Properties for the Transverse Direction

Steel	YS (MPa)	UTS (MPa)	YS/UTS (–)	UE (Pct)	TE (Pct)	$n_{2\text{-}4}$ (–)	TUE (–)	TFS (–)	TTS (–)	UTSxTE (MPa*Pct)
DP780	513	823	0.62	14.2	19.9	0.20	0.13	0.48	0.45	16378
TRIP780	542	851	0.64	20.7	25.8	0.20	0.19	0.49	0.25	21956
DP980	816	1055	0.77	6.54	9.7	0.13	0.06	0.57	0.57	10234
3rd Gen DP1180	895	1212	0.74	10.5	14.3	0.15	0.10	0.49	0.51	17332
3rd Gen TBF1180	987	1216	0.81	9.2	12.6	0.11	0.09	0.55	0.57	15322
3rd Gen Q&P1180	1034	1191	0.87	9.2	13.1	0.09	0.09	0.63	0.64	15602

YS yield stress, *UTS* ultimate tensile strength, *UE* uniform elongation, *TE* total elongation (initial gauge length of 80 mm), $n_{2\text{ to }4}$ strain hardening exponent between 2 and 4 pct deformation, *TUE* true uniform strain, *TFS* true fracture strain, *TTS* true thickness strain.

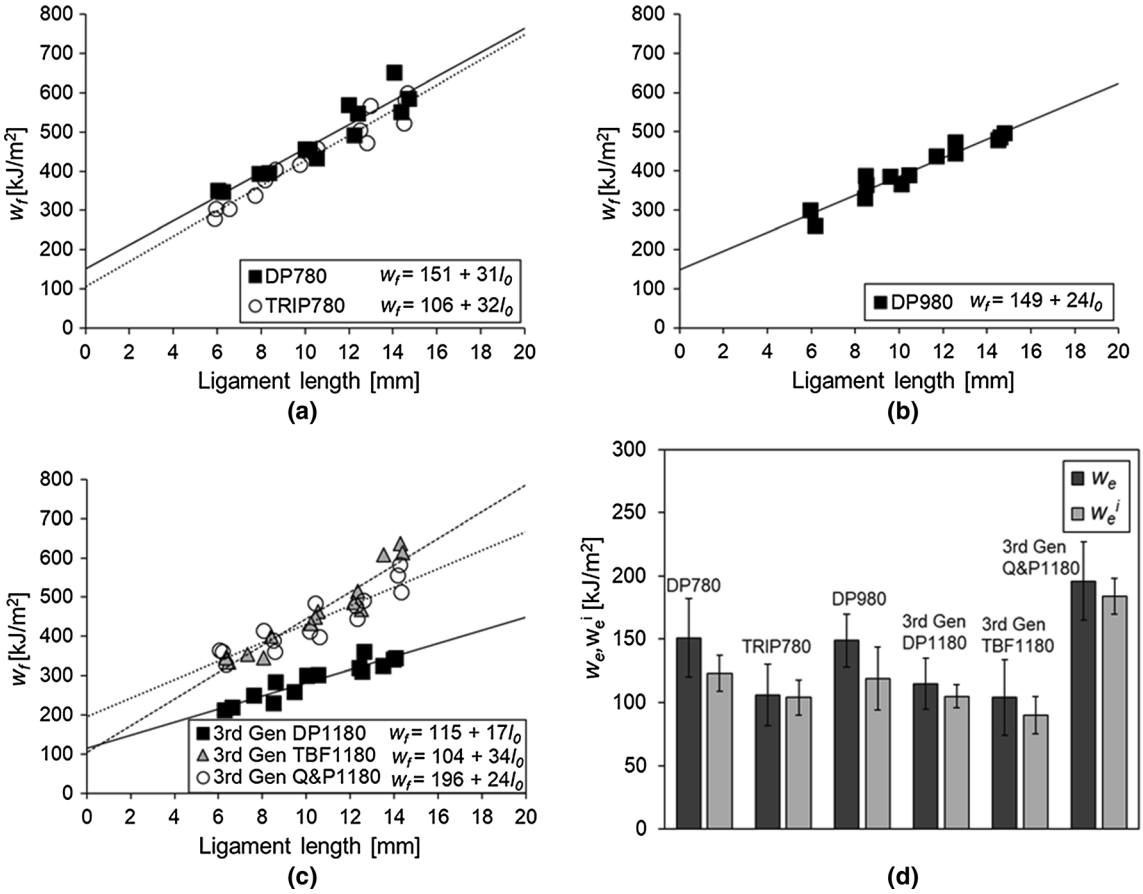

Fig. 8—w_f as a function of the ligament length (l_0) for: (*a*) 780 MPa, (*b*) 980 MPa, and (*c*) 1180 MPa steel grades. (*d*) w_e and w_e^i for all the investigated AHSS grades.

Table V. Results from EWF Tests and HET

	EWF		Thickness Strain DENT		HET	
Steel	w_e^i (kJ/m^2)	w_e (kJ/m^2)	$\varepsilon_{3f\ DENT}^i$ (–)	$\varepsilon_{3f\ DENT}^p$ (–)	HER (Pct)	TTS_{HET} (–)
DP780	123 ± 14	151 ± 31	0.08 ± 0.01	0.17 ± 0.00	34 ± 3	0.11 ± 0.03
TRIP780	104 ± 14	106 ± 24	0.07 ± 0.00	0.14 ± 0.01	23 ± 3	0.08 ± 0.00
DP980	119 ± 25	149 ± 21	0.08 ± 0.01	0.11 ± 0.01	38 ± 1	0.11 ± 0.02
3rd Gen DP1180	105 ± 9	115 ± 20	0.05 ± 0.00	0.10 ± 0.01	32 ± 1	0.10 ± 0.02
3rd Gen TBF1180	90 ± 15	104 ± 30	0.06 ± 0.01	0.10 ± 0.03	28 ± 2	0.11 ± 0.02
3rd Gen Q&P1180	184 ± 14	196 ± 31	0.09 ± 0.02	0.14 ± 0.02	41 ± 4	0.12 ± 0.01

DP1180, and 3rd Gen TBF1180 have slightly lower w_e^i than DP780 and DP980 while 3rd Gen Q&P1180 shows the greatest w_e^i. DP780 and DP980 present the highest contribution from crack propagation resistance after initiation ($w_e^i/w_e \approx 0.80$). In 3rd Gen DP1180 and 3rd Gen TBF1180 steels, such contribution is lower ($w_e^i/w_e \approx 0.90$). For the steels TRIP780 and 3rd Gen Q&P1180, the energy for crack initiation represents 0.98 and 0.94 of the total fracture energy, respectively.

2. *Fracture thickness strain from DENT specimens*

Thickness strain of DENT specimens is plotted in Figure 9 as a function of the distance from the crack tip. $\varepsilon_{3f\ DENT}^i$ and $\varepsilon_{3f\ DENT}^p$ values are summarized in Figure 9(d) and Table V.

$\varepsilon_{3f\ DENT}^i$ corresponds to the value of $\varepsilon_{3f\ DENT}$ at the crack tip (distance from crack tip = 0 mm). As observed in Figures 9(a) through (c), $\varepsilon_{3f\ DENT}$ reaches a constant value, corresponding to the stable crack propagation, around 0.4 to 0.5 mm from the crack tip. $\varepsilon_{3f\ DENT}^p$ is an average of $\varepsilon_{3f\ DENT}$ for a crack tip distance between 0.4 and 0.8 mm.

The steels DP780, TRIP780, DP980, and 3rd Gen Q&P1180 present similar thickness strain at crack initiation ($\varepsilon_{3f\ DENT}^i \approx 0.08$). 3rd Gen DP1180 and 3rd Gen TBF1180 show lower $\varepsilon_{3f\ DENT}^i$ (≈ 0.05). DP780 also

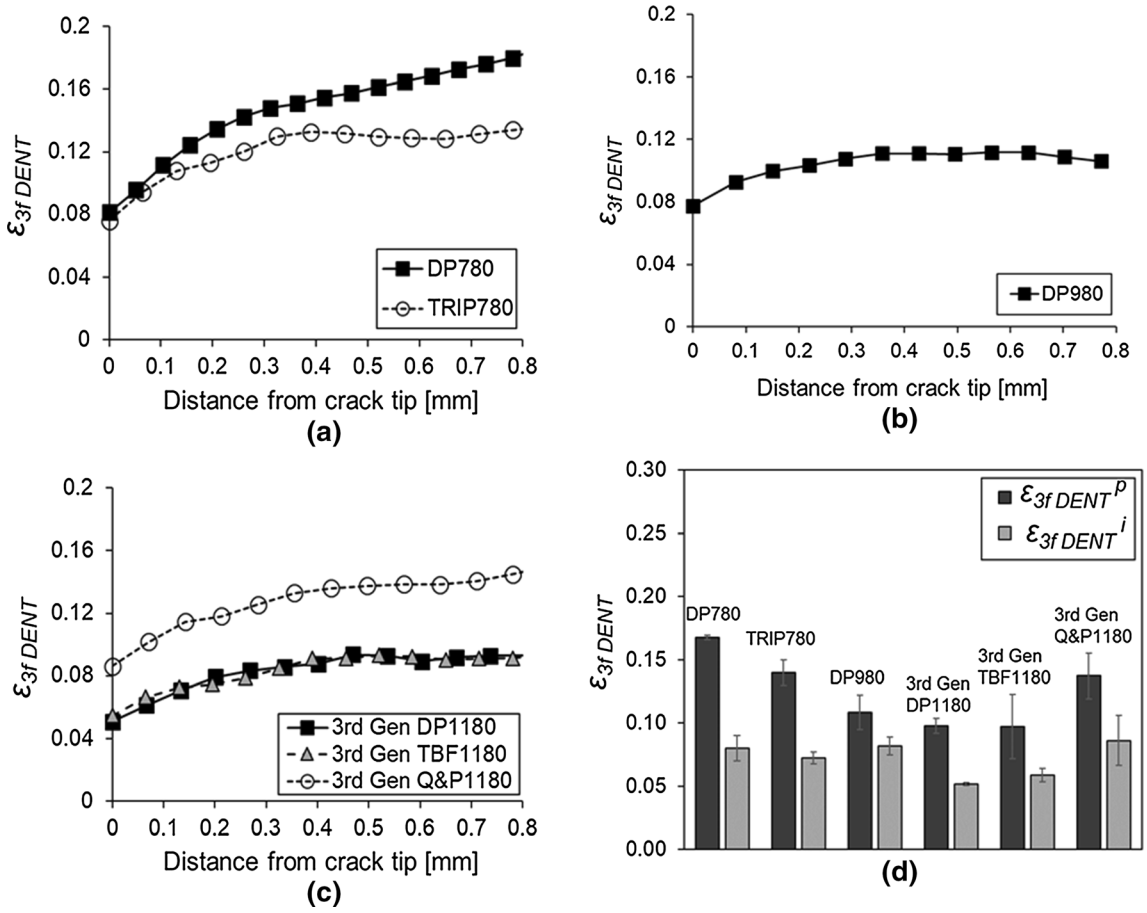

Fig. 9—$\varepsilon_{3f\ DENT}$ as a function of the distance from the crack tip for (*a*) 780 MPa, (*b*) 980 MPa, and (*c*) 1180 MPa steel grades. (*d*) $\varepsilon^{i}_{3f\ DENT}$ and $\varepsilon^{p}_{3f\ DENT}$ for all the investigated AHSS grades.

exhibits the greatest thickness strain for the crack propagation, followed by 3rd Gen Q&P1180 and TRIP780. Finally, DP980, 3rd Gen DP1180, and 3rd Gen TBF1180 present the lowest $\varepsilon^{p}_{3f\ DENT}$.

C. *Hole Expansion Tests*

The measured HER values are shown in Figure 10(a) and Table V. The results are the average of 5 specimens. The standard deviation is indicated (error bars). The Q&P steel exhibits the greatest HER, followed by DP980 and DP780. The latter shows very similar HER as 3rd Gen DP1180 and 3rd Gen TBF1180. The TRIP780 steel presents the lowest HER among the investigated steels.

In Figures 10(b) through (d), the thickness strain measured from HET specimens is plotted as a function of the distance from the punched hole edge. Because of the lower thickness in the shear-affected zone (SAZ), the values of thickness strain are higher near the hole edge. After an initial transition, the thickness strain stabilizes at a distance of approximately 0.5 to 0.6 mm from the edge. To avoid the influence of the SAZ in thickness measurements, thickness strain for HET specimens was determined for a distance between 0.5 and 1.5 mm. The values of true thickness strain in HET specimens (TTS_{HET}) are summarized in Table V.

Small differences can be appreciated in TTS_{HET} for the investigated AHSS grades. Most of the steels (DP780, DP980, 3rd Gen DP1180, and 3rd Gen TBF1180) present similar thinning at fracture in HET specimens ($TTS_{HET} \approx 0.11$). 3rd Gen Q&P1180 and TRIP780 show the highest and lowest TTS_{HET}, respectively.

IV. DISCUSSION

A. *Effect of the Microstructure on Mechanical Properties and Fracture Resistance*

The mechanical properties of AHSS are closely related to their complex multiphase microstructures. The two investigated 780 MPa steel grades, DP780 and TRIP780, have similar microstructures consisting of a ferritic–bainitic matrix with the presence of martensite islands and different RA contents. The greater content of RA in TRIP780 leads to higher uniform and total elongation compared to DP780 (Figure 7), thanks to the contribution of the TRIP effect. The beneficial influence of TRIP effect on mechanical properties is associated with the formation of additional geometrically necessary

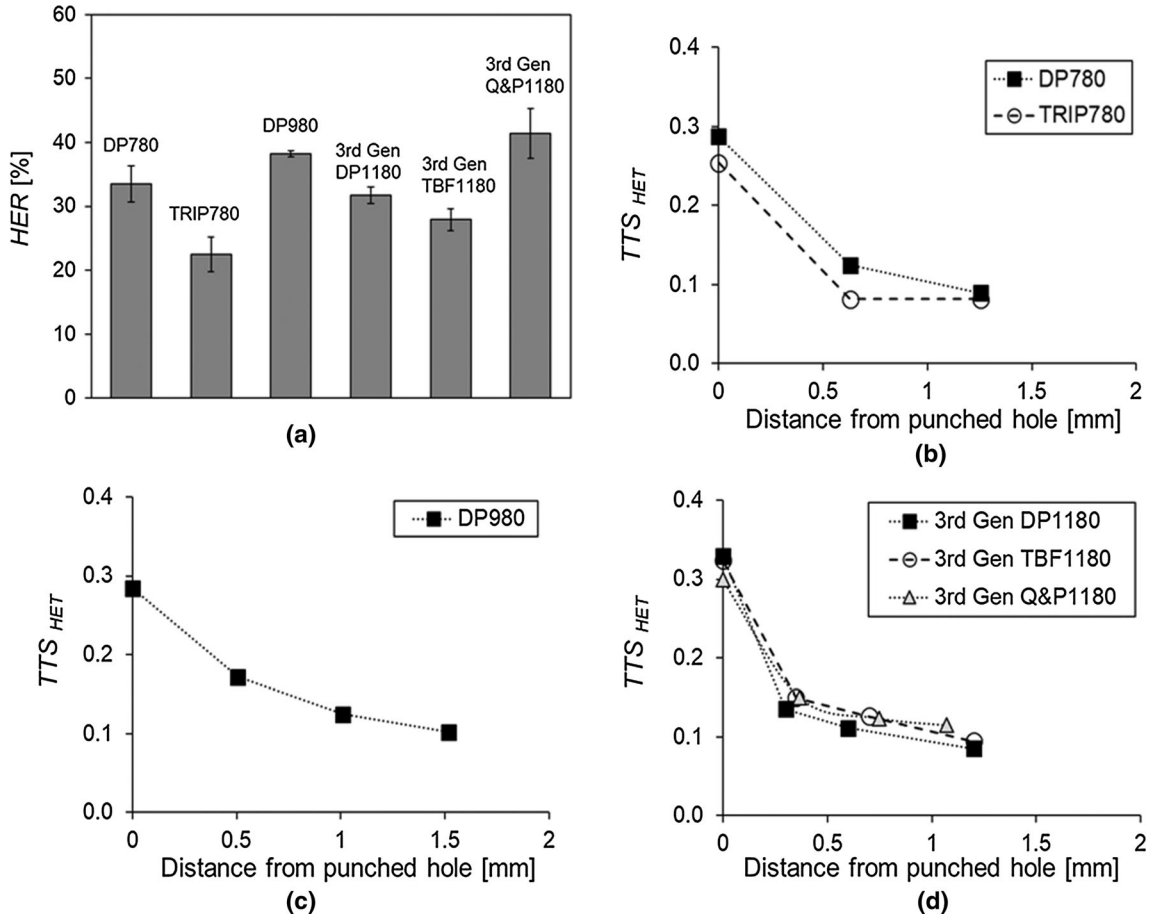

Fig. 10—(*a*) Hole expansion ratio values for the investigated AHSS grades. (*b* through *d*) Thickness strain near the crack measured from HET specimens.

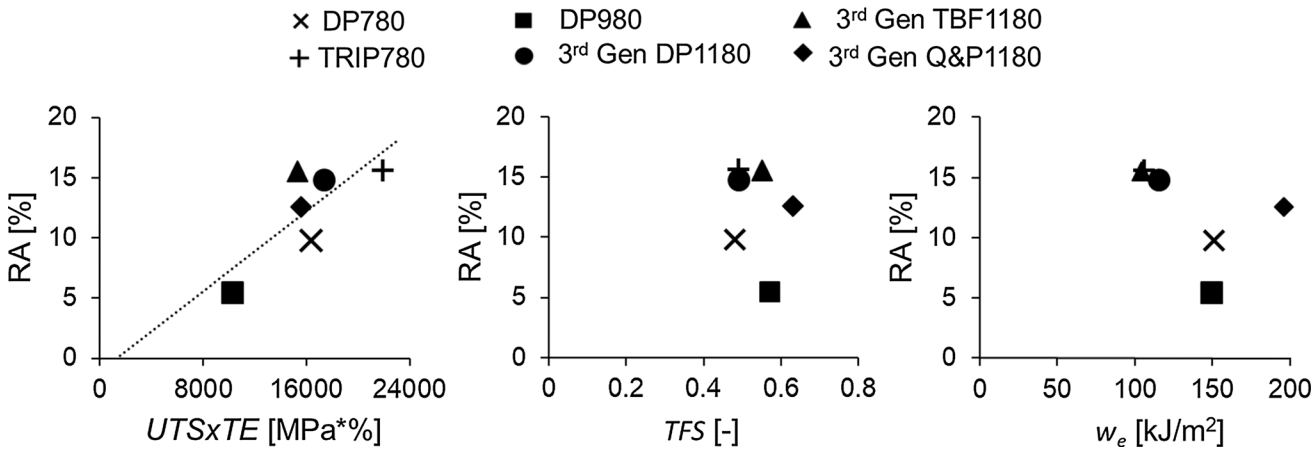

Fig. 11—Relation of RA content with strength/ductility and fracture resistance parameters.

dislocations during the strain-induced martensitic transformation, which increases work hardening and delays the onset of necking.[55,56] The amount of dislocations generated depends on the amount of the RA transformed. Therefore, a higher RA volume fraction implies a higher contribution of the TRIP effect to the mechanical performance. The relation between the RA content and uniaxial tensile strength and ductility is illustrated in Figure 11; the higher the RA content, the higher the UTSxTE product.

In DP980, part of the ferrite is replaced by tempered martensite and the amount of martensite is increased with respect to DP780 and TRIP780, resulting in higher strength and lower elongation. DP980 has the lowest

amount of RA. Therefore, the contribution of the TRIP effect to the uniform and total elongation is limited compared to the other steel grades. The substitution of the soft ferrite by bainite or tempered martensite in 3rd Gen 1180 MPa steels allows attainment of higher strength levels, while the strain-induced transformation of RA to martensite significantly improves the ductility compared to DP980.

The advantageous effect of RA and the strain-induced transformation to martensite on strength and ductility has been reported in several works.[55,57–60] Nevertheless, the contribution of TRIP effect to fracture resistance is not so evident as shown in Figure 11. The figure shows no direct correlation of RA volume fraction with the TFS or the fracture toughness (w_e). For instance, looking at 1180 MPa steel grades, it can be seen that the 3rd Gen Q&P1180 shows the highest TFS and w_e, whereas it has the lowest amount of RA. The same applies for 780 MPa steel grades. Despite the larger RA content of TRIP780, it shows similar TFS and lower w_e than DP780. This finding points out the limited, or even negative, impact of RA on edge formability and crash performance.

Xiong *et al.*[60] also observed that, for a Q&P steel quenched at different temperatures, the UTSxTE product increased with increasing the RA content, while fracture toughness decreased. This detrimental effect of RA on cracking resistance is attributed to the higher stress triaxiality present in the crack tip which significantly increases the RA to martensite transformation rate. Consequently, the brittle network of fresh martensite created in the fracture process zone favors damage and rapid crack propagation.[59,60] Different studies revealed that other factors, such as the RA morphology, size, or stability, also have influence on fracture resistance of TRIP-assisted steels.[48,59–61]

However, fracture resistance is not only controlled by RA content and stability but also by matrix characteristics and secondary phases distribution. The work of de Diego-Calderon *et al.*[61] showed that crack initiation in Q&P steels is mainly controlled by the tempered martensite grain size and volume fraction, which increases the plastic strain energy to form micro-ductile structures and by the untempered martensite island formed during Q&P cycle, which act as cleavage initiation sites. According to this, the larger amount of fresh martensite present in the 3rd Gen DP1180 probably has a negative effect on TFS and w_e. On the other hand, the more homogeneous carbon-depleted martensite matrix of 3rd Gen Q&P1180 contributes to increase the fracture resistance. Therefore, to obtain an optimum balance between fracture resistance and global formability, the RA volume fraction and stability as well as the matrix characteristics should be carefully controlled.

B. *Correlation Between Stretch Flangeability and Fracture Resistance Parameters*

The identification of the material properties governing the stretch flangeability of AHSS has been the focus of extensive research.[14,17,28–33,51] As mentioned before, the HER has become the most widespread parameter for stretch flangeability and edge cracking resistance assessment of AHSS. However, while it is a very useful parameter for material ranking, it is not an intrinsic material property and depends on many variables. For this reason, constant efforts are devoted to correlate the HER with mechanical properties. Contrary to the observations for low strength steels,[62] conventional uniaxial tensile properties such as tensile strength or elongation are not good indicators of HER. This is also shown in Figure 12, where the HER values measured in this work are plotted against different tensile properties (UE, TE, UTSxTE) and fracture resistance parameters (TFS, TTS, w_e). The figure shows that the HER decreases with increasing UE, TE, and UTSx UTE product, which is opposite to the initial expectations. On the other hand, fracture resistance parameters such as the TFS, the TTS, or the w_e are more suitable to rationalize stretch flangeability of AHSS, *i.e.,* the higher the fracture resistance, the higher the stretch flangeability. An especially good linear correlation is observed between HER and w_e ($R^2 = 0.79$), which is in good agreement with the results of Casellas *et al.*[14] and Frómeta *et al.*[15] For the sake of comparison, the w_e and HER values obtained in this work are plotted, together with the results of References 14 and 15, in Figure 13. Unpublished results for different HSLA steels are also included. The very good linear fitting for different AHSS families ($R^2 = 0.91$) strengthen the hypothesis that stretch flangeability of AHSS is mainly dictated by fracture toughness, measured here in terms of w_e, which controls the propagation of the microcracks generated during hole punching (or edge cutting). It is important to remark that HER values do not only depend on material properties but also on hole preparation method, edge quality, *etc.* Consequently, deriving definitive conclusions only from HETs may sometimes lead to misleading material ranking and non-optimum material selection. In turn, fracture toughness is the material property that controls cracking resistance and represents a more objective design parameter for microstructural optimization in terms of fracture resistance.

C. *Thickness Strain Measurements*

Figure 14 compares the thickness strains measured in HET, DENT, and uniaxial tensile specimens. For all the investigated AHSS grades, the values of thinning measured in HET specimens (TTS_{HET}) are within the range of thickness strain measurements from DENT specimens ($\varepsilon_{3f}^{i}{}_{DENT}$ and $\varepsilon_{3f}^{p}{}_{DENT}$). It suggests that fracture mechanisms involved in HET and DENT tests are phenomenologically similar; *i.e.,* in both tests, fracture is triggered by the propagation of pre-existing cracks (microcracks around the punched hole in HET,[14,33] and fatigue pre-cracks in DENT specimens). Accordingly, the critical thinning for edge crack propagation can be directly related to the thickness strains measured in pre-cracked DENT specimens, as shown in Figure 14.

This approach can be seen as an alternative to the edge thinning limit (ETL) criterion proposed by Hance.[54] The ETL is defined as the critical thinning

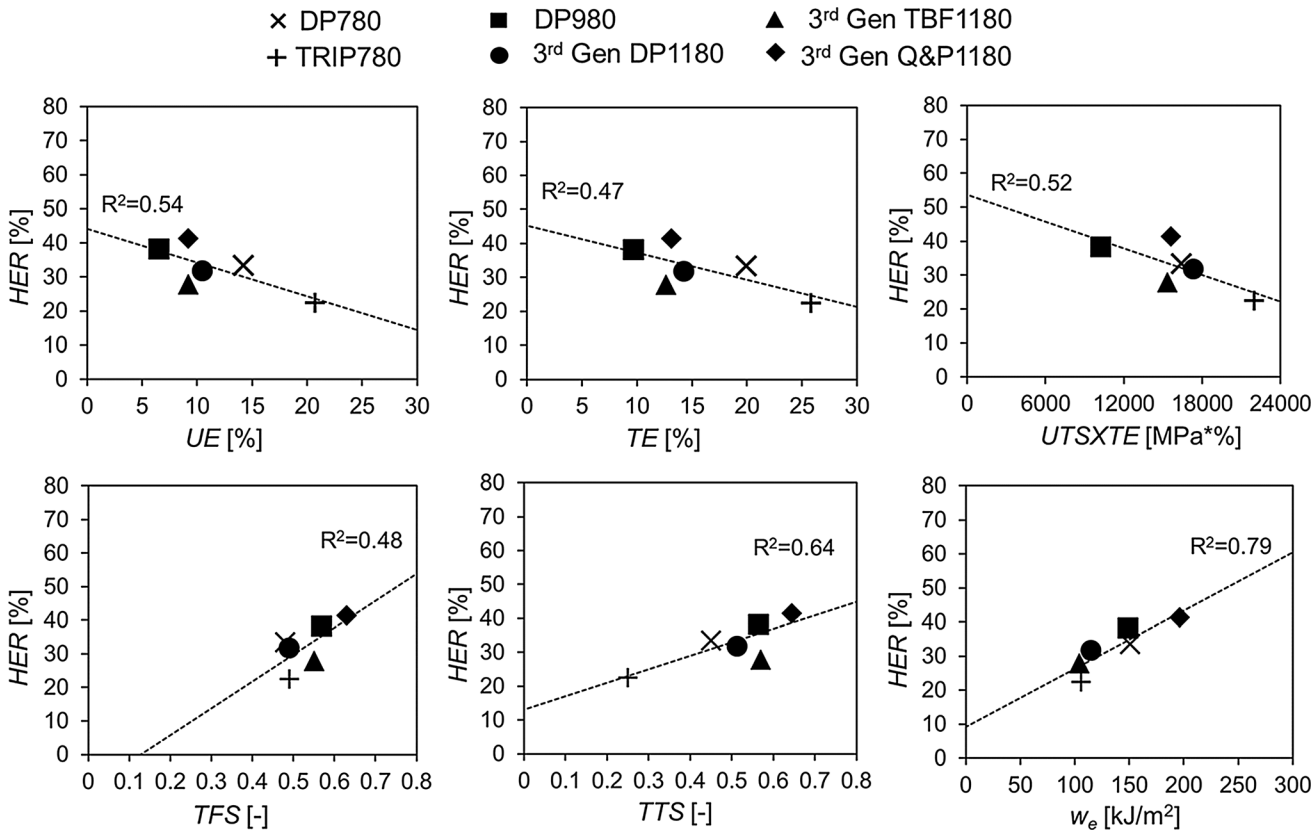

Fig. 12—HER values as a function of different uniaxial strength/ductility and fracture resistance parameters.

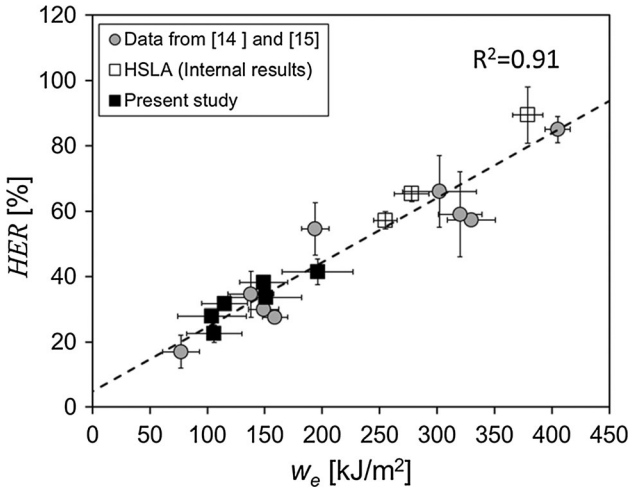

Fig. 13—Correlation between HER and w_e for the AHSS grades investigated in this work together with previously published results by the authors.[14,15] Internal unpublished results for HSLA are also plotted. All the HER values shown are from HETs according to ISO16630.

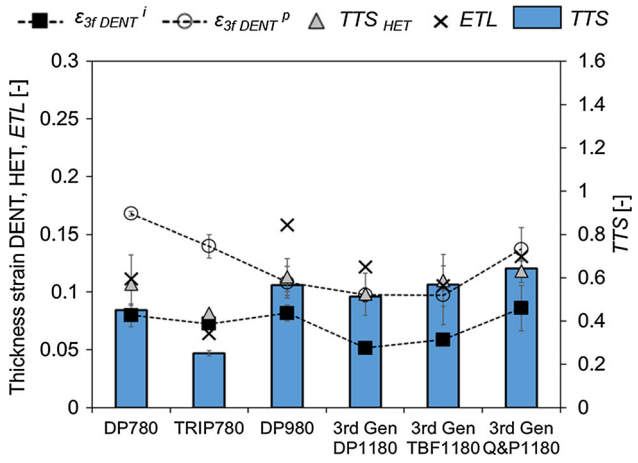

Fig. 14—Thickness strain measurements performed in DENT, HET, and uniaxial tensile specimens. Edge thinning limit (*ETL*) values are also plotted.

for edge crack propagation and is calculated according to Eq. [9]:

$$\mathrm{ETL} = 1 - \exp\left[\frac{-\ln\left(1 + \left(\frac{\mathrm{HER_{LB}}}{100}\right)\right)}{R_\mathrm{m} + 1}\right] \qquad [9]$$

where $\mathrm{HER_{LB}}$ is the lower-bound HER[54] and R_m is the normal anisotropy.

If the ETL is exceeded anywhere along the edge of a deformed blank, or a punched hole in this case, then there is high risk of edge cracking. Figure 14 plots the calculated ETL values for the steels investigated in the present work. As observed, ETL values are in good agreement with $\mathrm{TTS_{HET}}$ and $\varepsilon_{3f\ \mathrm{DENT}}$. Therefore, thickness strain measurements in pre-cracked DENT

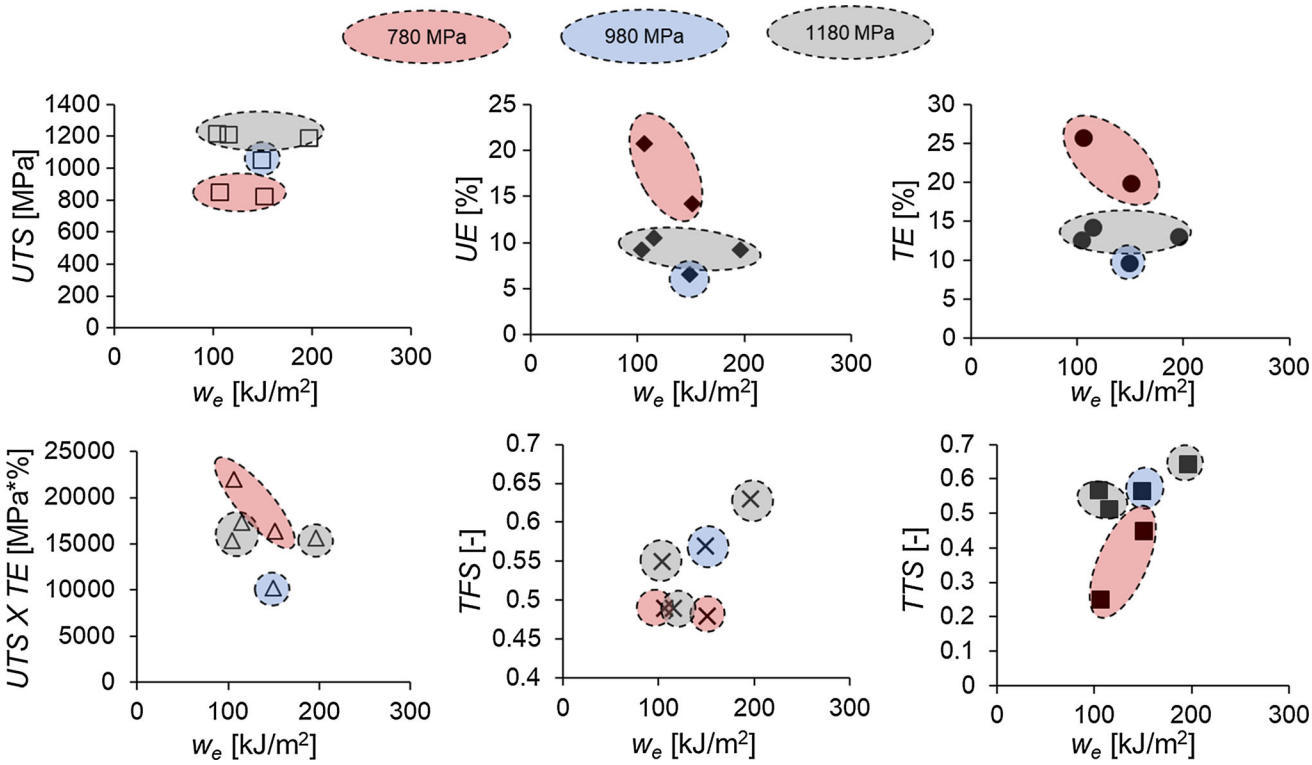

Fig. 15—Correlation between fracture toughness and uniaxial tensile properties.

specimens can be used to establish a limit edge crack thickness strain which, like the ETL criterion, can be implemented in FEM software as an objective and physically motivated criterion for edge-cracking prediction. Establishing a comparison between this criterion and the edge thinning diagram proposed by Hance,[54] the lower safe limit for edge crack prediction would be dictated by the $\varepsilon^{i}_{3f\ DENT}$. Below this thickness strain, the component would be safe from edge cracking. The upper limit for failure would be given by DENT $\varepsilon_{3f\ DENT^{P}}$. The range between $\varepsilon^{i}_{3f\ DENT}$ and $\varepsilon^{p}_{3f\ DENT}$ would indicate risk of cracking.

As shown in Figure 14, the values of TTS from uniaxial tensile specimen completely overestimate the thickness strains from DENT and HET specimens (TTS = 0.25 to 0.64). However, looking at the relative differences between the different steel grades, it can be observed that the thickness strain values for the three different test configurations follow a similar trend. This evidences that, whereas the TTS cannot be directly used to estimate the thickness reduction in DENT and HET specimens, it can provide a qualitative ranking in terms of fracture toughness and edge fracture resistance.

These observations may help to better understand the relationship between edge fracture and crack propagation resistance in AHSS. However, other factors such as the influence of cutting or punching conditions on limit edge thinning values should be investigated in further detail to define a reliable fracture criterion for edge crack prediction, considering initial edge damage and crack propagation resistance.

D. *Relation Between Tensile Properties and Fracture Toughness*

As discussed above, fracture toughness is a relevant property to assess the fracture resistance of AHSS. Unfortunately, as shown in Figure 15, there is no a direct relationship between fracture toughness and conventional uniaxial tensile properties.[48,51,60] It is clearly shown that elongation values (uniform and total) or the UTSxTE products, which is usually used as a toughness indicator, are not suitable parameters to estimate the cracking resistance of AHSS. On the other hand, as previously observed for edge fracture resistance (Figure 12), local strain measurements from uniaxial tensile tests (TFS, TTS) give a better estimation of fracture toughness. Nevertheless, previous works showed that these fracture-related parameters often cannot accurately describe the fracture behavior of the material when it is related to the presence of existing cracks or defects.[51,60] Therefore, to better understand the fracture performance of AHSS sheets, including crack initiation and propagation resistance, fracture toughness should be properly measured in the frame of fracture mechanics.

E. *AHSS Classification According to Their Crack Propagation Resistance*

The need for new classification mappings based on formability and fracture performance of AHSS has become more and more evident in the last years.[16,17,30,31] The concept of a global/local

formability map for AHSS was introduced by Hance,[16] who proposed a novel diagram for AHSS performance classification. The global formability was represented in terms of uniform elongation, which is a suitable measure of the material resistance against strain localization or necking, and local formability was indexed on the basis of the TFS. The ratio between uniform strain and TFS provides a general idea about the overall formability of the material. Alternatively, Larour *et al.*[30] and Heibel *et al.*,[31] suggested the use of the true thickness strain (TTS), for local formability prediction, based on the good correlation between TTS and HER. Heibel *et al.*[31] stated that thickness strain measurements are more accurate than fracture strains based on the reduction of area (TFS or *Z*-value), since they do not take into account the fracture width, which is only influenced by global formability. They developed a formability mapping using the TTS and the true uniform strain (ε_u) as a measure of local and global formability, respectively.

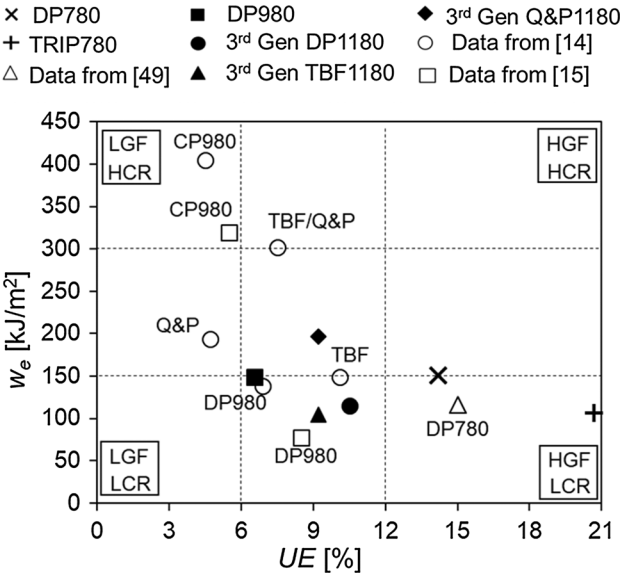

Fig. 16—AHSS classification based on global formability (UE) and fracture resistance (w_e). *LGF* low global formability, *LCR* low cracking resistance, *HGF* high global formability, *HCR* high cracking resistance.

However, none of these classification approaches consider the material's crack propagation resistance which, as shown in the present work and in previous publications,[14,15,34,35,51] provides useful information about the overall fracture behavior of AHSS sheets. According to this, an alternative performance mapping approach accounting for the crack propagation resistance is proposed in Figure 16. The figure plots the uniform elongation (UE) in the *x*-axis and the specific essential work of fracture (w_e) in the *y*-axis. The specific essential work of fracture is raised as an index of local formability or cracking resistance, *i.e.*, the higher the w_e, the higher the cracking resistance. The diagram is divided into different quadrants according to global and local formability levels. The more to the right in the plot the greater the global formability, whereas upper quadrants indicate superior fracture resistance and damage tolerance. Compared to traditional classification diagrams based only on tensile strength and elongation values, such as the so-called banana plot (Figure 17a), this classification system allows a more complete description of the formability and fracture performance of AHSS (Figure 17b). Moreover, it can serve as a guide for future steel development and optimum material selection for automotive structural parts.

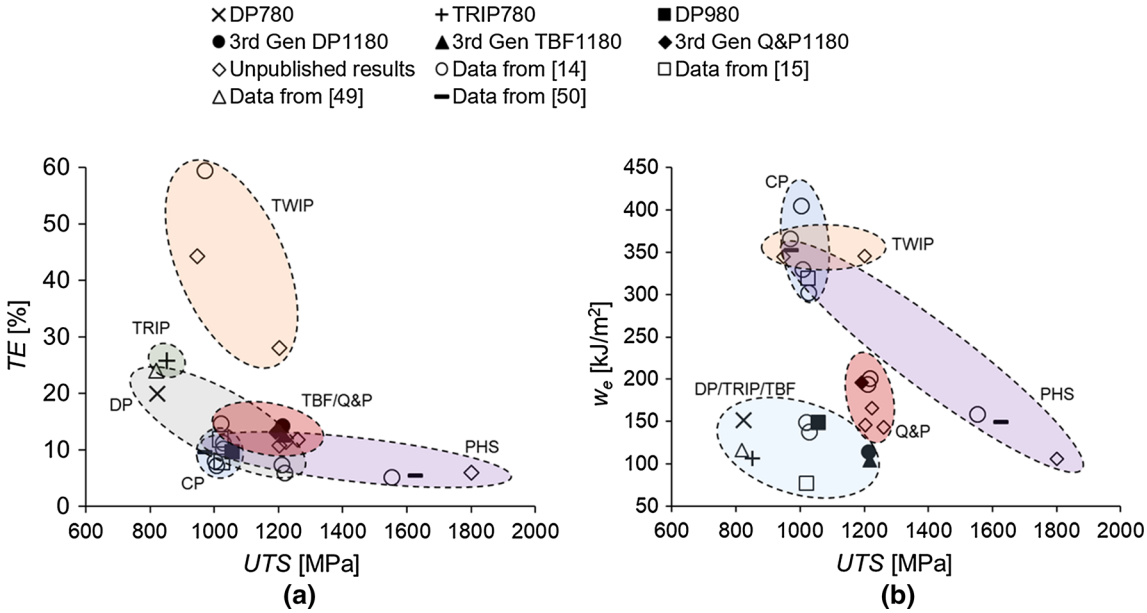

Fig. 17—(*a*) Conventional classification diagram of AHSS steels ("banana plot") in terms of UTS and *TE*. (*b*) Proposed diagram for classification of AHSS according to their strength level (UTS) and fracture resistance (w_e).

V. CONCLUSIONS

The mechanical properties and the fracture resistance of different 1st- and 3rd-generation AHSS grades have been investigated. From the analysis of the obtained results, the following conclusions can be drawn:

- Conventional uniaxial tensile properties are not sufficient to describe the local formability and fracture behavior of AHSS. On the other hand, other fracture-related parameters such as the true fracture strain (TFS), the true thickness strain (TTS), or the specific essential work of fracture (w_e) provide a better prediction of fracture performance. The very good correlation between w_e and HER values for several AHSS and HSLA steels consolidates the observations made in previous work and confirms the close relationship between fracture toughness and stretch flangeability in AHSS.
- A new classification mapping considering global ductility (UE) and fracture resistance (w_e) is proposed for a more exhaustive description of the overall formability and fracture behavior of AHSS. The proposed diagram can be useful for improved AHSS performance ranking and optimum material selection depending on the requirements of the intended application.
- The true thickness strain (TTS) from uniaxial tensile tests significantly overestimates the thickness reduction in punched hole edge and fatigue pre-cracked DENT specimens. However, the relative differences in TTS are well reflected in toughness and edge cracking resistance parameters. Therefore, it might be used as a qualitative indicator of fracture toughness and edge fracture resistance.
- The values of thickness strain measured in fatigue pre-cracked DENT specimens ($\varepsilon_{3f\ DENT}$) are similar to edge thinning values measured in HET specimens (TTS_{HET}). This evidences the similarity between edge fracture and crack propagation mechanisms and allows establishing an objective fracture criterion for edge-cracking prediction. These results highlight the importance of addressing edge cracking phenomena considering the underlying fracture mechanisms, since fracture is governed by crack propagation resistance.
- The essential work of fracture is proposed here as a relevant parameter to assess the fracture resistance of AHSS and to understand the role of microstructural constituents on fracture behavior. The investigation on the correlation between fracture toughness and uniaxial tensile properties has shown that fracture toughness cannot be estimated from traditional ductility or toughness indicators (UE, TE, UTSxTE, etc.). Local strain measurements from tensile tests (TFS, TTS) offer a better estimation of fracture toughness. However, none of these parameters can accurately describe the fracture behavior in the presence of cracks. Therefore, fracture toughness, understood as the material's crack initiation and propagation resistance, must be measured following a fracture mechanics approach to properly evaluate the microstructural effects on fracture behavior.
- The results obtained from fracture toughness tests revealed that microstructural features that improve global ductility, such as the TRIP effect, can have a detrimental effect on fracture toughness. Hence, microstructural design must take into account not only tensile properties but also crack initiation and propagation resistance parameters.

ACKNOWLEDGMENTS

This work has been financially supported by the European Commission, Research Fund for Coal and Steel programme under Grant Agreement 800693 — CrashTough — RFCS-2017.

FUNDING

Open access funding provided by Lulea University of Technology.

REFERENCES

1. S. Keeler, M. Kimchi, and P.J. Mooney: Advanced High-Strength Steels Application Guidelines, version 6.0, 2017.
2. WorldAutoSteel: FutureSteelVehicle—final engineering report. https://steel.org/~/media/Files/Autosteel/Programs/FutureSteelVehicle/FSV%20-%20Final%20Engineering%20Report.pdf, 2011.
3. E. Billur and T. Altan: *Stamp. J.*, 2013, pp. 16–17.
4. E. Billur, J. Dykeman, and T. Altan: *Stamp. J.*, 2014, pp. 12–13.
5. C. Liu, Q. Peng, Z. Xue, S. Wang, and C. Yang: *Materials*, 2018, vol. 11, p. 2242.
6. H.L. Yi: *JOM-J. Min. Met. Mat. S.*, 2014, vol. 66, pp. 1759–69.
7. D. Raabe, D. Ponge, O. Dmitrieva, and B. Sander: *Scr. Mater.*, 2009, vol. 60, pp. 1141–44.
8. K. Mori, Y. Abe, and Y. Suzui: *J. Mater. Process. Technol.*, 2010, vol. 210, pp. 653–59.
9. D. Frómeta, M. Tedesco, J. Calvo, A. Lara, S. Molas, and D. Casellas: *J. Phys: Conf. Ser.*, 2017, vol. 896, p. 012102.

10. C.R.M. Silva, F.J.G. Silva, and R.M. Gouveia: *Procedia Manuf.*, 2018, vol. 17, pp. 737–45.
11. A. Karelova, C. Krempaszky, E. Werner, P. Tsipouridis, T. Hebesberger, and A. Pichler: *Steel Res. Int.*, 2009, vol. 80, pp. 71–77.
12. F. Hisker, R. Thiessen, and T. Heller: *Mater. Sci. Forum*, 2012, vols. 706–709, pp. 925–30.
13. P. Efthymiadis, S. Hazra, A. Clough, R. Lakshmi, A. Alamoudi, R. Dashwood, and B. Shollock: *Mater. Sci. Eng. A*, 2017, vol. 701, pp. 174–86.
14. D. Casellas, A. Lara, D. Frómeta, D. Gutiérrez, S. Molas, L.L. Pérez, J. Rehrl, and C. Suppan: *Metall. Mater. Trans. A*, 2017, vol. 48, pp. 86–94.
15. D. Frómeta, A. Lara, S. Parareda, and D. Casellas: *AIP Conf. Proc.*, 2019, vol. 2113, p. 160007.
16. B. Hance: *Proceedings of the International Automotive Body Congress (IABC)*, 2016, Dearborn, Michigan.
17. S. Heibel, T. Dettinger, W. Nester, T. Clausmeyer, and A.E. Tekkaya: *Materials*, 2018, vol. 11, p. 761.
18. ISO 16630:2017. Metallic Materials—Sheet and Strip—Hole Expanding Test. *International Organization for Standardization.*.
19. M. Schneider and U. Eggers: *Proceedings of the International Deep Drawing Research Group* (IDDRG) conference, 2011, Bilbao, Spain, June 5–8, 2011.
20. E. Atzema, M. Borsutzki, M. Braun, S. Brockmann, M. Bülter, B. Carlsson, P. Larour, and A. Richter: *New Development in Sheet Metal Forming 2012 International Conference*. Fellbach, Germany, May 23–24, 2012, pp. 171–84.
21. B. Hance, R. Comstock, and D. Scherrer: *SAE Technical Paper*, 2013, 2013-01-1167.
22. P. Larour, H. Pauli, J. Freudenthaler, J. Lackner, F. Leomann, and G. Schestak: *Proceedings of the International Deep Drawing Research Group (IDDRG) Conference*, 2016, Linz, Austria, June 12–15, 2016, pp. 480–96.
23. E. Levin, P. Larour, M. Heuse, D. Staupendahl, T. Clausmeyer, and A.E. Tekkaya: *IOP Conf. Ser.: Mater. Sci.*, 2018, vol. 418, p. 012061.
24. P. Larour, J. Freudenthaler, A. Grünsteidl, and K. Wang: *Proceedings of the International Deep Drawing Research Group (IDDRG) Conference*, 2014, Paris, France, June 1–4, 2014, pp. 188–93.
25. J. Dykeman, S. Malcolm, B. Yan, J. Chintaman, G. Huang, N. Ramisetti, and H. Zhu: *SAE Technical Paper*, 2011, 2011-01-1058.
26. P. Larour, H. Schauer, J. Lackner, and E.T. Till: *Proceedings of the International Deep Drawing Research Group (IDDRG) 2016 Conference*. Linz, Austria, June 12–15, 2016, pp. 457–59.
27. G Huang, K Tihay, S Sriram, B Weber, P Dietsch, and D Cornette: *IOP Conf. Ser.: Mater. Sci. Eng.*, 2018, vol. 418, p. 012080.
28. S Westhäuser, M Schneider, M Teschner, and IA Denks: *IOP Conf. Ser.: Mater. Sci. Eng.*, 2019, vol. 651, p. 012049.
29. I.A. Denks, M. Schneider, S. Westhäuser, and C. Lesch: *Steel Res. Int.*, 2019, vol. 90 (6), p. 1800460.
30. P. Larour, J. Freudenthaler, and T. Weissböck: *J. Phys.: Conf. Ser.*, 2017, vol. 896, p. 012073.
31. B. Hance: *SAE Int. J. Mater. Manf.*, 2018, vol. 11 (4), pp. 505–16.
32. Y. Takahashi, O. Kawano, and Y. Tanaka: *MS&T 2009: Proceedings from the Materials Science & Technology Conference*. October 25–29, 2009, Pittsburgh, Pennsylvania, pp. 317–1328.
33. J.I. Yoon, J. Jung, S.H. Joo, T.J. Song, K.G. Chin, M.H. Seo, S.J. Kim, S. Lee, and H.S. Kim: *Matter. Lett.*, 2016, vol. 180, pp. 322–26.
34. D. Frómeta, A. Lara, S. Molas, D. Casellas, J. Rehrl, C. Suppan, P. Larour, and J. Calvo: *Eng. Fract. Mech.*, 2019, vol. 205, pp. 319–32.
35. D. Frómeta, A. Lara, B. Casas, and D. Casellas: *IOP Conf. Ser. Mater. Sci. Eng.*, 2019, vol. 651, p. 012071.
36. E. Wirthl, A. Pichler, R. Angerer, P. Stiaszny, K. Hauzenberger, Y. Titovets, and M. Hackl: *Proceedings of the International Conference on TRIP-Aided High Strength Ferrous Alloys*, Gent, Belgium, 2002.
37. ISO 6892-1:2009 (2009) Metallic materials—tensile testing—Part 1: method of test at room temperature. *European Committee for Standardization.*
38. ASTM E8/E8M-15a: *Standard Test Methods for Tension Testing of Metallic Materials*, ASTM International, West Conshohocken, PA, 2015.
39. B. Cotterell and J.K. Reddel: *Int. J. Fract.*, 1977, vol. 13, pp. 267–77.
40. Y.W. Mai and B. Cotterell: *Int. J. Fract.*, 1986, vol. 32, pp. 105–25.
41. J. Wu and Y.W. Mai: *Polym. Eng. Sci.*, 1996, vol. 36, pp. 2275–88.
42. A.B. Martínez, J. Gamez-Perez, M. Sanchez-Soto, J.I. Velasco, and O. Santana: M. Ll. Maspoch*Eng. Fail. Anal.*, 2009, vol. 16, pp. 2604–17.
43. Y.W. Mai and K.M. Pilko: *J. Mater. Sci.*, 1979, vol. 14, pp. 386–94.
44. Y.W. Mai and B. Cotterell: *J. Mater. Sci.*, 1980, vol. 13, pp. 2296–2306.
45. T. Pardoen, Y. Marchal, and D. Delannay: *J. Mech. Sol.*, 1999, vol. 47, pp. 2093–2123.
46. Y. Marchal and F. Delannay: *Int. Fract. J.*, 1996, vol. 80, pp. 295–310.
47. B. Cotterell, T. Pardoen, and A.G. Atkins: *Eng. Fract. Mech.*, 2005, vol. 72, pp. 827–48.
48. G. Lacroix, T. Pardoen, and P.J. Jacques: *Acta Mater.*, 2008, vol. 56, pp. 3900–13.
49. D. Gutiérrez, L.L. Pérez, A. Lara, D. Casellas, and J.M. Prado: *19th European Conference on Fracture: Fracture Mechanics for Durability, Reliability and Safety, ECF 2012.*
50. S. Golling, D. Frómeta, D. Casellas, and P. Jonsén: *Mater. Sci. Eng. A*, 2019, vol. 743, pp. 529–39.
51. D. Frómeta, S. Parareda, A. Lara, S. Molas, D. Casellas, P. Jonsén, and J. Calvo: *Eng. Fract. Mech.*, 2020, vol. 229, p. 106949.
52. Z. Xiong, P.J. Jacques, A. Perlade, and T. Pardoen: *Int. J. Fract.*, 2020, vol. 224, pp. 101–16.
53. E. Clutton: Essential work of fracture, in *Fracture Mechanics Testing Methods for Polymers, Adhesives and Composites*, vol. 28, D.R. Moore, A. Pavan, J.G. Williams, eds., ESIS Publ., 2001, pp. 177–195.
54. B. Hance: *SAE Int. J. Engines*, 2017, vol. 10 (2), pp. 247–57.
55. P. Jacques, Q. Furnémont, A. Mertens, and F. Delannay: *Philos. Mag. A*, 2001, vol. 81, pp. 1789–1812.
56. D. Krizan, K. Steineder, S. Kaar, and T. Hebesberger: *19th International Scientific Conference Transfer 2018*, Trencianske Teplice (Slovakia).
57. G.B. Olson and M. Cohen: *Metall. Trans. A*, 1975, vol. 6, p. 791.
58. G.B. Olson and M. Azrin: *Metall. Trans. A*, 1978, vol. 9, pp. 713–21.
59. P. Jacques, Q. Furnémont, T. Pardoen, and F. Delannay: *Acta Mater.*, 2001, vol. 49, pp. 139–52.
60. Z. Xiong, P.J. Jacques, A. Perlade, and T. Pardoen: *Metall. Mater. Trans. A*, 2019, vol. 50, pp. 3502–13.
61. I. de Diego-Calderón, I. Sabirov, J.M. Molina-Aldareguia, C. Föjer, R. Thiessen, and R.H. Petrov: *Mater. Sci. Eng. A*, 2016, vol. 657, pp. 136–46.
62. X. Chen, H. Jiang, Z. Cui, C. Lian, and C. Lu: *Proc. Eng.*, 2014, vol. 81, pp. 718–23.